RSC Advances

PAPER

View Article Online
View Journal | View Issue

Cite this: *RSC Adv.*, 2025, **15**, 10700

Alumina-supported highly dispersed platinum–copper nanocatalyst with good dehydrogenation performance for perhydromonobenzyltoluene as a hydrogen carrier†

Qiuyue Ding,[a] Yixuan Zhang,[b] Huijie Wei,[b] Qing Li,[b] Yanyan Xi,[c] Songqing Hu*[a] and Xufeng Lin *[bd]

Precious metal catalysts are widely used in the field of heterogeneous catalysis in general and, in particular, for the dehydrogenation process of liquid organic hydrogen carriers (LOHCs). However, improving their catalytic activity and selectivity simultaneously is challenging owing to the characteristics of transition metals. Herein, a catalyst, namely, $Pt_{2.5}Cu_{0.1}/Al_2O_3$-H_2, was developed that could break the negative correlation between catalytic activity and selectivity, improving the overall dehydrogenation performance and reducing costs. This method achieved highly dispersed nanoparticles (NPs) and co-localization to form a unique $PtCu_x$ alloy with reduced Pt electron density by anchoring low loadings of Cu-doped Pt on an alumina support. It also suppressed strong metal support interactions (SMSIs), as confirmed by characterization results such as XPS and HRTEM, resulting in excellent bimetallic synergistic catalytic dehydrogenation activity and selectivity in perhydromonobenzyltoluene (12H-MBT), compared with $Pt_{2.6}/Al_2O_3$-H_2. The reaction energy barrier for the dehydrogenation of 12H-MBT was relatively low (~94 kJ mol^{-1}), and the rate-determining step of the whole catalytic dehydrogenation was identified to be 4H-MBT → 0H-MBT.

Received 16th January 2025
Accepted 6th March 2025

DOI: 10.1039/d5ra00385g

rsc.li/rsc-advances

Introduction

As the global community confronts dual challenges of decarbonization and energy security optimization, it is urgent to explore renewable and environmentally friendly clean energy sources. Hydrogen energy is believed to have a significant role in the future energy systems.[1,2] Safe and effective storage is one of the most critical factors restricting the development of efficient hydrogen utilization. Various hydrogen storage technologies have been widely studied, such as the high-pressure gaseous hydrogen storage, low-temperature liquid hydrogen storage and solid material hydrogen storage technologies. However, they still have their own drawbacks in the long-distance and large-scale hydrogen transportation,[3] and the method based on liquid organic hydrogen carriers (LOHCs) can be a solution to this problem. With the LOHC-based method, reversible catalytic hydrogenation/dehydrogenation reactions of oil-like compounds can be carried out under mild conditions,[4] endowing the advantages of high hydrogen storage capacity, good safety, and compatibility with the existing fuel infrastructure.[5] At present, various LOHCs have been extensively studied, such as cyclohexane, methylcyclohexane (MCH), and dibenzyltoluene (DBT). These LOHCs have standard hydrogenation preparation technologies and are used at an industrial level. However, there are some limiting factors in dehydrogenation, such as slow hydrogen evolution kinetics rate, high dehydrogenation temperature, and low selectivity.[6–8] Monobenzyltoluene (0H-MBT), having lower viscosity than DBT, has huge potential in hydrogen storage application. In addition to its large theoretical hydrogen storage capacity (6.17 wt%), it has the characteristics of a suitable dehydrogenation temperature (below 563 K), low volatility, safety and non-toxicity.[9]

The key to improving the competitiveness of the MBT-based hydrogen storage technique is to solve the problems of high dehydrogenation temperature, side reactions, and poor stability. To date, precious metal catalysts, such as Pt, Pd, and Ru, have been confirmed to be effective in the dehydrogenation process of common aromatic compounds.[10–12] Especially, Pt-based catalysts have good potential in improving the

[a]College of Material Science and Engineering, China University of Petroleum (East China), 266580, Qingdao, P. R. China. E-mail: ccupc@163.com
[b]College of Chemistry and Chemical Engineering, China University of Petroleum (East China), 266580, Qingdao, P. R. China. E-mail: hatrick2009@upc.edu.cn
[c]Advanced Chemical Engineering and Energy Materials Research Center, China University of Petroleum (East China), 266580, Qingdao, P. R. China
[d]State Key Laboratory of Heavy Oil Processing, China University of Petroleum (East China), 266580, Qingdao, P. R. China

† Electronic supplementary information (ESI) available. See DOI: https://doi.org/10.1039/d5ra00385g

dehydrogenation performance of 12H-MBT. For example, Kwak *et al.*[13] investigated the dehydrogenation performance of different hydrogen carriers (MCH, 12H-MBT, and 18H-DBT) on a 0.5 wt%-Pt/γ-Al_2O_3 catalyst at 280–340 °C. It was found that the dehydrogenation rate of 12H-MBT at 270 °C was only about 52%, while the cost could significantly increase if high loadings of precious metals were used. To solve the above-mentioned problems, appropriate approaches include adding a second metal component, changing the support and modifying the preparation process. In terms of support replacement, the Wasserscheid's research group[14] compared the performance of Pt catalysts using C, Al_2O_3, and SiO_2 as supports in the 12H-MBT and 18H-DBT systems. They found that the dehydrogenation rate of Pt/C (5 wt%) for the former was 87% at 270 °C. However, for 12H-MBT, relatively few catalyst improvement methods are available for reference, which can be obtained from other hydrogen carriers. For example, Guo *et al.*[15] improved the anti-coking ability of a Cu–Pt alloy formed by doping Cu into Pt/S-1, resulting in a conversion rate of 92.26% for MCH dehydrogenation. Wang *et al.*[16] prepared bimetallic PdCu/r-GO catalysts loaded with reduced graphene oxide in different ratios. The $Pd_{1.2}Cu$/rGO catalyst achieved 100% selectivity for the final dehydrogenation product of *N*-ethylcarbazole at 453 K. The amount of Pd was reduced by more than 60% compared to the typical commercial and reported catalysts. Shi *et al.*[17] also investigated the effect of Pt/Al_2O_3 with surface hydroxyl groups and surface oxygen vacancies obtained by plasma treatment on the reversible hydrogenation and dehydrogenation reactivity of 18H-DBT. Corma *et al.*[18] compared the effect of the Pt/NaY zeolite catalyst samples with different metal dispersions on the dehydrogenation efficiency of MCH. The aim was to explore the relationship between the catalyst structure and catalytic activity. To date, the kinetics and mechanisms of cyclic hydrogenation and dehydrogenation of common aromatic compounds such as MCH, 12H-NEC, and 18H-DBT have also been relatively well deliberated.[19–21] For 12H-MBT, the hydrogenation technology is relatively well-established, and the catalytic hydrogenation mechanism is also rather well understood.[22,23] However, apart from the relatively few explorations on catalytic performance, there is also a lack of detailed research on the mechanism of catalytic dehydrogenation. This presents a challenge in hydrogen storage technology with respect to the system-dehydrogenation process.

To overcome these problems, this study employed a preparation strategy of anchoring and confinement of low-loading Pt-based alumina catalysts modified with a small amount of Cu. It achieved highly dispersed nanoscale metal particles, formed a unique $PtCu_x$ alloy and suppressed strong metal–support interactions (SMSI).[24] This strategy involved further calcination and fixation of the Pt–Cu precursor. For 12H-MBT, this catalyst exhibited an excellent bimetallic synergistic effect on dehydrogenation activity and product selectivity, which was superior to the previously reported precious metal catalyst.[15] The structure of the target catalyst was systematically characterized using high-resolution transmission electron microscopy (HRTEM) and X-ray photoelectron spectroscopy (XPS). The reaction mechanism, in particular, the rate-determining step of the 12H-MBT dehydrogenation, is discussed based on the characterization and kinetic results.

Experimental section

Chemicals

Monobenzyltoluene was purchased from Hubei Xinkang Pharmaceutical Chemical Co., Ltd and used as a hydrogenation reactant. $H_2PtCl_6 \cdot 6H_2O$, imidazolidinyl urea, methanal, ethylene glycol, sodium hydrate and dichloromethane were purchased from Sinopharm Group Chemical Reagent Co., Ltd. $Cu(NO_3)_2 \cdot 3H_2O$ was purchased from Shanghai Maclin Biochemical Technology Co., Ltd. Aluminium oxide and Ru/Al_2O_3 were purchased from Shaanxi Ruike New Material Co., Ltd. All atmospheres used are of ultra-pure grade (>99.99%).

Catalyst preparation

Equal-volume impregnation method with hydrogen reduction post-treatment. Alumina calcined in the muffle furnace at 500 °C for 4 h was used as the catalytic support. Additionally, 0.265 g of $H_2PtCl_6 \cdot 6H_2O$ and 0.015 g of $Cu(NO_3)_2 \cdot 3H_2O$ were dissolved in 3.6 ml of deionized water to form the precursor solution of the target product. Then, the precursor solution was added to the 4 g of roasted alumina support and subjected to vacuum immersion for 12 hours. The above sample, aged for 1 hour, was dried at 120 °C for 2 hours, and then further calcined at 500 °C for 4 hours. Finally, the sample was heated to 500 °C in H_2 (40 ml min^{-1}) and reduced for 4 h. The obtained catalyst was denoted as $Pt_{2.5}Cu_{0.1}/Al_2O_3$-H_2 (the subscript numbers represent weight percentages, wt%). Similarly, the metal ratio was varied to obtain different loadings of Pt–Cu catalysts, which were named accordingly.

Equal volume impregnation with pre-coordination and methanal reduction (MR). The precursor solution of the $Pt_{2.0}Cu_{0.1}/Al_2O_3$-H_2 catalyst was sonicated for 1 hour during the preparation process, then an appropriate amount of imidazolidinylurea (with the same molar amount of metal) was added. After drying the above samples, add the following solution and reduce them at 75 °C for 4 hours. The solution treatment process was as follows: 60 ml of formaldehyde was added to a solution mixed with 40 ml of ethylene glycol and 40 ml of deionized water, and the pH value was adjusted to about 11 by adding 0.1 mol per L NaOH. Finally, the $Pt_{2.5}Cu_{0.1}$-Al_2O_3-MR catalyst was obtained, and similarly, other catalysts with different metal ratios were also be prepared.

Catalyst characterization

The sample composition and crystallinity data were obtained using the D8 Advance XRD X-ray powder diffractometer. The X-ray source was tested under the conditions of a Cu target (40 kV, 40 mA, $\lambda = 0.1541$ nm), ranging from 4.5° to 90°, step size of 0.02° and operating power of 2.2 kW.

The specific surface area, pore volume, and maximum pore size of the sample catalysts were analyzed using the Micromeritics ASAP 2460 BET automatic adsorption instrument. It

was tested using high-purity nitrogen in a liquid nitrogen ultra-low temperature environment.

High-resolution transmission electron microscopy (HRTEM) imaging analysis was performed on the samples using the JEOL JEM-F200 electron microscope, Japan.

The morphology of the samples was analyzed using SEM-EDX on the German ZEISS GeminiSEM 300 ultra-high resolution field emission scanning electron microscope. The energy spectrum mapping tests were operated using an energy spectrometer (Smartedx) to observe the element distributions and contents.

The X-ray photoelectron spectroscopy (XPS) test required the use of the American Thermo Scientific K-Alpha X-ray source. After taking the appropriate amount of the sample and pressing it onto the sample disk, the sample was placed into the sample chamber. When the pressure in the sample chamber was less than 2.0×10^{-7} mbar, the sample was tested at a spot size of 400 μm, working voltage of 12 kV and filament current of 6 mA. Eventually, the peaks in the spectrum obtained from the above tests were analyzed based on the external reference value of 284.9 eV for the C 1s peak and were rectified for charge effects.

H_2-TPD testing on the samples was performed using the American Micromeritics AutoChem II 2920 chemical adsorption instrument. Firstly, 0.1 g of the sample was fixed in a quartz tube and preprocessed in a H_2 (50 ml min^{-1}) atmosphere at 300 °C for 2 h to dislodge the passivation behavior on the surface of the metal particles. It was blown for 1 hour with He (50 ml min^{-1}) and cooled at 50 °C. Secondly, a 10% H_2/Ar mixture (50 ml min^{-1}) was introduced for 1 h until saturation, and the Ar air flow (50 ml min^{-1}) was switched to blow for 1 h to remove weak H_2 physical adsorption on the surface. Finally, the gas was desorbed at a heating rate of 10 °C min^{-1} to 600 °C in an Ar atmosphere, and the desorbed gas was detected using a Thermal Conductivity Detector (TCD). The CO chemical adsorption capacity was measured by the CO pulse on the HP chemical adsorption instrument. Firstly, 0.2 g of the sample was placed in a U-tube reactor, reduced at 300 °C in a H_2/Ar flow (50 ml min^{-1}) for 2 h and cooled to room temperature. Then, it was pulsed multiple times with CO (50 ml min^{-1}) in the Ar air flow and the chemical adsorption signal of CO was detected using a TCD detector until there was no chemical adsorption signal of CO. The CO chemisorption capacity was quantified through pulse chemisorption measurements. Pt nanoparticle dispersion was quantified *via* pulse chemisorption analysis.

The CO Fourier diffuse reflectance infrared spectroscopy (CO-DRIFT) was performed using a Thermo iS10 spectrometer. The testing process was as follows: firstly, the sample was subjected to a H_2 flow (50 ml min^{-1}) for 2 h at 300 °C before CO adsorption. The background spectrum of the sample could be collected when the sample was cooled to room temperature under a N_2 flow (50 ml min^{-1}). Subsequently, the CO flow rate of 50 ml min^{-1} was added to the spectral cell to allow the sample to adsorb for 30 minutes and reach saturation. Then, the sample was cleaned continuously with N_2 at a flow rate of 50 ml min^{-1} until the infrared signal of the sample stopped changing and the CO-DRIFT spectra were collected. Furthermore, the 12H-MBT DRIFT test was conducted on a Bruker INVENIO-S infrared spectrometer, Germany. First, the sample was placed in an *in situ* cell and pretreated in an H_2 flow (50 ml min^{-1}) at 300 °C for 2 hours to eliminate partial oxidation behavior on the surface of the metal particles. Then, the background spectrum of the sample could be collected after cooling the sample in N_2 flow (50 ml min^{-1}) to room temperature. Spectra were collected after saturating the N_2 mixture (60 ml min^{-1}) containing 12H-MBT at room temperature. Then, the sample was heated at a rate of 5 °C min^{-1} to the given temperature (220, 230, 240, 250, 260 °C) for 180 seconds before sequentially collecting the corresponding spectral signals. All spectra required background subtraction to highlight the reaction adsorption spectral signal of 12H-MBT.

The dehydrogenation test of 12H-MBT and its reaction kinetics

Preparation of 12H-MBT. 12H-MBT was prepared by the complete hydrogenation of 0H-MBT. 30.0 g of MBT as the reactant and 3.0 g of 5 wt% Ru–Al_2O_3 catalyst were added and reacted with pure H_2 for 2 hours in an autoclave equipped with a mechanical stirrer. The reaction conditions were 413 K, 5 Mpa, and 600 rpm. 0H-MBT could be completely hydrogenated to afford the product 12H-MBT (≥99%) under the reaction conditions described above.[25] The elemental analysis of the reaction product was used to further confirm the successful preparation of 12H-MBT (C : H = 6.4 : 1).

Dehydrogenation performance of 12H-MBT. Similarly, 20.0 g of the as-prepared 12H-MBT and 2.0 g of Pt_yCu_z/Al_2O_3-H_2/MR catalysts (*y* and *z* denoted as the mass loadings of Pt and Cu in percentages, respectively) were added to an autoclave equipped with a condenser and a H_2 gas outlet connected by a flow meter. The above dehydrogenation reaction was carried out at 260 °C, atmospheric pressure, and a stirring rate of 600 rpm. Similarly, while maintaining the above reaction conditions unchanged, 50.0 g of the as-prepared 12H-MBT and 5.0 g of the $Pt_{2.5}Cu_{0.1}$-Al_2O_3-H_2 catalyst were reacted at different temperatures (220, 230, 240, 250, 260 °C) as the kinetic experiments. The composition of the dehydrogenation products was determined by a gas chromatograph (Agilent 7820A) and a gas chromatography-mass spectrometer (PE CLARUS 680 + SQ8). The release of hydrogen was recorded by an electronic display flow recorder, which is referenced in the experimental equipment documentation and related calculation formulas.

The calculation method of some quantities of interest is described here. The dehydrogenation performance was represented as the degree of dehydrogenation (DoD), which is related to the degree of hydrogenation (DOH), as shown in (1) and (2), respectively. These were defined as the ratio of the amount of hydrogen stored in the LOHC to its maximum potential hydrogen storage capacity of LOHC.[26] Moreover, the selectivity of the full dehydrogenation product, *i.e.*, 0H-MBT, could be expressed as the total degree of dehydrogenation (TDoD). The activation energy of the apparent dehydrogenation reaction of the system was obtained by the Arrhenius formula, as shown in eqn (3). In eqn (3), *k* represents the reaction rate constant, *R* is

the molar gas constant (8.314 J mol^{-1} K^{-1}), T is the absolute temperature of the reaction and A is the pre factor.[27] Turnover frequency (TOF) is an important measure of the intrinsic activity of the catalyst. It reliably reflected the reaction initiation phase.[28] TOF could be expressed by formula (4), where $r \cdot AC$ is the rate constant for the consumption of 12H-MBT per minute per gram catalyst (mol min^{-1} g_{cat}^{-1}), n_{total} is the molar mass of Pt and D is the active site dispersion per gram of the catalyst (g_{cat}^{-1}).[29]

$$\mathrm{DoH} = \frac{n_{H_2,max} - n_{H_2,released}}{n_{H_2,max}} \quad (1)$$

$$\mathrm{DoD} = 1 - \mathrm{DOH} \quad (2)$$

$$\ln k = \frac{-E_a}{RT} + \ln A \quad (3)$$

$$\mathrm{TOF} = \frac{r \cdot \mathrm{AC}}{n_{total} \cdot D}. \quad (4)$$

Results and discussion

Catalyst characterization of basic physiochemical properties

As shown in Fig. 1, modification of the Pt/Al_2O_3 catalyst with a small amount of Cu doping was to achieve a low-cost catalyst with high dispersion and small particle size. It could have a bimetallic synergistic effect and weaken SMSI to some extent. Extensive analyses were conducted in order to examine the differences between the $Pt_{2.5}Cu_{0.1}/Al_2O_3$-H_2 catalyst with the alloy synergistic effect, pure Pt and other Pt–Cu bimetallic catalysts. It further investigated the factors responsible for the synergistic effect between Pt and Cu. The characterization results of the basic physical and chemical properties of the prepared catalyst are shown in Fig. S1, S2, Tables S1 and S2 of the first part of the ESI.† The characterization results closely related to the bimetallic synergistic effect are shown below.

Characterization of the metal component properties

XPS spectroscopy was used to analyze the chemical state changes of the Pt–Cu and pure Pt catalysts with different preparation methods. The XPS spectra of Pt 4f and Cu 2p (Fig. 2a and b) showed that Pt mainly existed in a metallic state in the catalyst. The asymmetric peaks in the energy spectra with binding energies ranging from 70.0 to 70.3 eV and 74.1 to 74.9 eV correspond to Pt. The Pt $4f_{5/2}$ binding energy (74.8 eV) of Pt atoms in the $Pt_{2.5}Cu_{0.1}/Al_2O_3$-H_2 catalyst was slightly higher than that of Pt atoms in the $Pt_{2.6}/Al_2O_3$-H_2 (74.6 eV)[30] and the $Pt_{2.5}Cu_{0.1}/Al_2O_3$-MR (74.7 eV) catalysts. These indicated that the addition of Cu contributed to the partial electron transfer of Pt, which carried partial positive charges ($Pt^{\delta+}$). In addition, compared with Pt and Cu catalysts prepared by formaldehyde reduction, the number of electrons transferred from Pt atoms to Cu increased slightly, and the electron density of Pt decreased. The electronegativity of Cu atoms was larger, making it easier to catalyze hydrogen absorption synergistically. Due to the low loading of Cu in both catalysts, the weak intensity peaks at the binding energies of ~931.6–933.7 eV and ~952.4–953.8 eV were attributed to the Cu $2p_{3/2}$ and Cu $2p_{1/2}$, respectively.[31] Here, the Cu $2p_{3/2}$ binding energy (931.6 eV) in $Pt_{2.5}Cu_{0.1}/Al_2O_3$-H_2 was lower than that of Cu $2p_{3/2}$ in the $Pt_{2.5}Cu_{0.1}/Al_2O_3$-MR catalyst (933.7 eV). This further confirmed that some electrons in the Pt atoms in the Pt–Cu catalyst had transferred to Cu atoms, which confirmed the formation of the $PtCu_x$ alloy. Moreover, the Pt $4f_{5/2}$ binding energy (74.7 eV) of Pt atoms in $Pt_{2.5}Cu_{0.1}/Al_2O_3$-MR was slightly higher than that in the $Pt_{2.6}/Al_2O_3$-MR catalyst (74.5 eV). It indicated that the addition of Cu generated partial electron transfer between the Pt and Cu atoms as well. However, there was no significant electron transfer between the Pt and Cu atoms due to the absence of hydrogen reduction after calcination and fixation. It is worth mentioning that the Al 2p binding

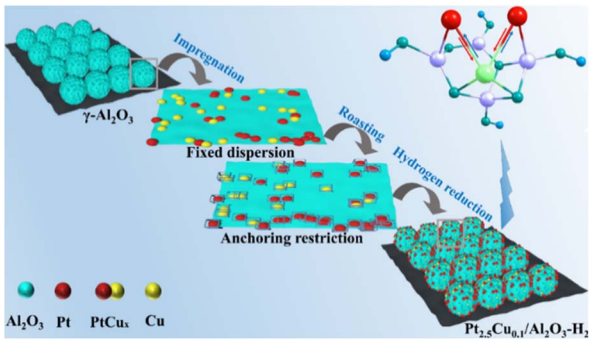

Fig. 1 Schematic diagram of the $Pt_{2.5}Cu_{0.1}/Al_2O_3$-H_2 catalyst preparation strategy process model of Al_2O_3 the Pt–Cu alloy NPs catalyst under pre-treatment roasting with Cu doping with spatial anchoring effect.

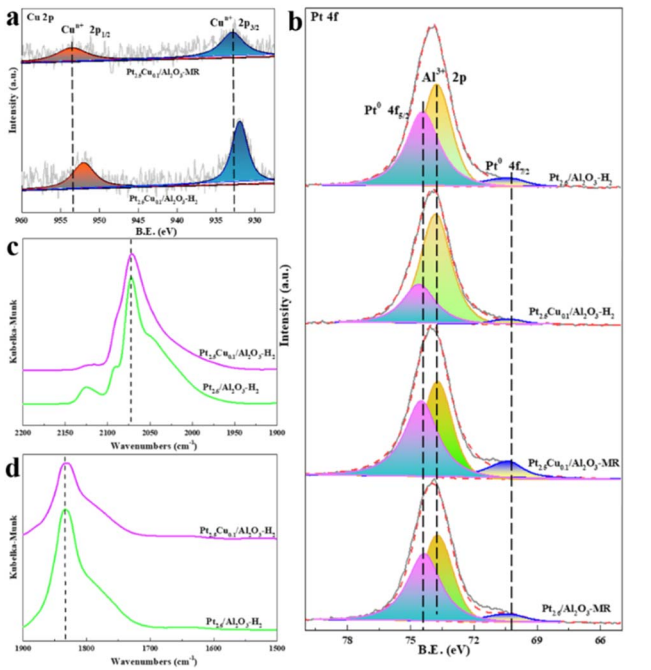

Fig. 2 XPS spectra of Cu 2p (a) and Pt 4f (b) on $Pt_{2.5}Cu_{0.1}/Al_2O_3$-H_2/MR and $Pt_{2.6}/Al_2O_3$-H_2/MR catalysts. (c and d) *In situ* CO-DRIFT spectra of $Pt_{2.5}Cu_{0.1}/Al_2O_3$-H_2 and $Pt_{2.6}/Al_2O_3$-H_2 catalysts.

energy of Al atoms in $Pt_{2.5}Cu_{0.1}/Al_2O_3$-H_2 was also higher than that in $Pt_{2.6}/Al_2O_3$-H_2, and the intensity of the characteristic peak was stronger. It was revealed that the addition of Cu formed an alloy structure, which also weakened the SMSI. Finally, the weakening effect of SMSI was more dominant than the electronic effect between Pt and Cu, resulting in an electron transfer between Pt and Cu.

The adsorption characteristics and electronic structure of Pt and Pt–Cu surfaces were investigated adopting the CO-DRIFT *in situ* spectroscopy at room temperature, as shown in Fig. 2c and d. In the $Pt_{2.5}Cu_{0.1}/Al_2O_3$-H_2 and $Pt_{2.6}/Al_2O_3$-H_2 samples, sharp peaks centered around ~2000–2100 cm^{-1} could be observed. These corresponded to the linear adsorption of CO molecules on the Pt (111) surface with a coordination number of 9.[32,33] The small peak extending to ~2125 cm^{-1} appeared in the $Pt_{2.6}/Al_2O_3$-H_2 sample, except for the narrow peak centered at 2067–2075 cm^{-1} in the $Pt_{2.5}Cu_{0.1}/Al_2O_3$-H_2 sample. This phenomenon was attributed to the linear adsorption of CO molecules at the low coordination edge and angle Pt sites and the relatively low adsorption strength of CO on this catalyst. The above behavior indicates that, on the one hand, Cu doped Pt catalysts increased the Pt exposure on the surface. It resulted in a more linear adsorption of CO molecules on the Pt (111) surface (combined with the CO chemisorption results). On the other hand, many studies have shown that inhibiting the adsorption of small molecules (such as CO and H_2) is the typical behavior in the presence of SMSI.[34] Meanwhile, the active center of Pt doped with Cu suppressed the interaction between the metal and the support (combined with XPS results). In addition, a peak centered at 1830–1850 cm^{-1} appeared, proving that the adsorption of CO in the $Pt_{2.5}Cu_{0.1}/Al_2O_3$-H_2 and $Pt_{2.6}/Al_2O_3$-H_2 samples was low adsorption. It meant that CO molecules were adsorbed between three Pt atoms, and the adsorption strength of the former was lower. It was related to the partial red shift of Pt with low coordination sites caused by a small amount of Cu doping occupying a certain amount of high coordination sites. These behaviors indicated that both were relatively small particle sizes, and the former had a larger particle size, making the CO molecule adsorption more difficult.[35,36]

In order to observe the interaction between the Pt and Cu particle sizes in the $Pt_{2.5}Cu_{0.1}/Al_2O_3$-H_2 sample, HRTEM was conducted, as shown in Fig. 3a. Among all the samples, the exposed surfaces of Al_2O_3 were mainly (110) surfaces. These illustrated that the catalyst supports were mainly γ-Al_2O_3. However, the exposed surfaces of Pt and Cu clusters were mainly (111) surfaces, which was related to the low loading of Cu, with little exposure of crystal planes. Meanwhile, it could be distinctly observed that numerous Pt nanoparticles (NPs) were directly loaded onto the γ-Al_2O_3 surface.[37,38] Compared with $Pt_{2.5}Cu_{0.1}/Al_2O_3$-MR, it could be seen that $Pt_{2.5}Cu_{0.1}/Al_2O_3$-H_2 had clearer alloy metal lattice stripes and higher dispersion of Pt and Cu particle sizes. This explained that the reduction of Pt and Cu was more stable and SMSI was also weaker. It was further certified that the synergistic catalytic effect of the catalyst was the combined result of interactions between the co-coordination of Pt and Cu and alloy formation (Fig. 3b). It was confirmed in DFT calculations, and the HRTEM results

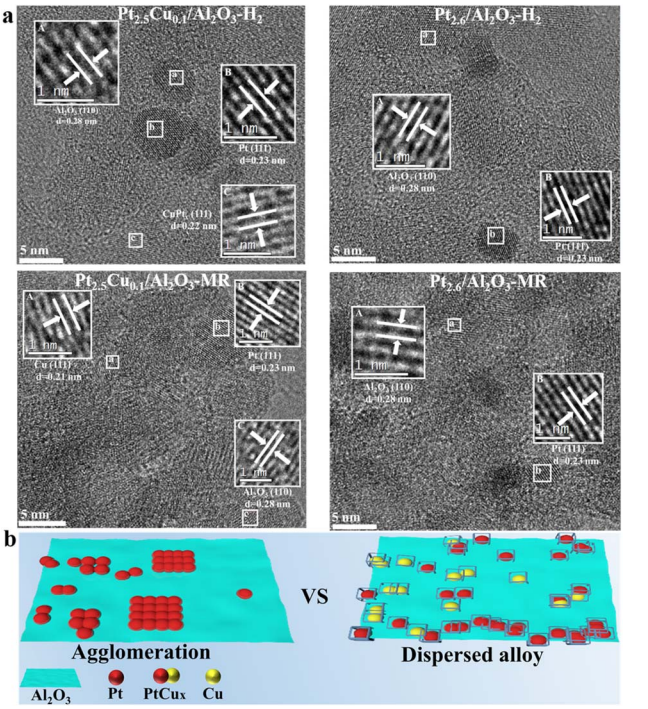

Fig. 3 (a) HRTEM images of $Pt_{2.5}Cu_{0.1}/Al_2O_3$-H_2/MR and $Pt_{2.6}/Al_2O_3$-H_2/MR catalysts. (b) Schematic structure of the $Pt_{2.5}Cu_{0.1}/Al_2O_3$-H_2 and $Pt_{2.6}/Al_2O_3$-H_2 catalysts from left to right, corresponding to HRTEM results, respectively.

further assisted the conclusions of XRD, BET, SEM, XPS, and CO-DRIFT (see the XRD, BET and SEM results in Fig. S1-A, S1-B and S1-E in ESI).†

The unique electron-transfer alloy structure of Pt–Cu in $Pt_{2.5}Cu_{0.1}/Al_2O_3$-H_2 could be the essential reason for the synergistic effect, showing high dehydrogenation activity and strong structural retention ability compared to the $Pt_{2.6}/Al_2O_3$-H_2 catalyst. On the other hand, the formation of a unique Pt–Cu electron transfer alloy structure is related to the high dispersion and nanoscale particles. This was obtained by hydrogen reduction after the Pt and Cu metal components are calcined and fixed. It is determined that its dehydrogenation activity far exceeds that of the catalyst obtained by liquid-phase reduction. In other words, adjusting the electron distribution between Pt and Cu by varying the proportions of the bimetallic precursors without significantly changing the size of Pt NPs could achieve the highly dispersed and alloyed state. Furthermore, further calcination of the precursor on the support also further anchors and limits the metal distribution, reducing SMSI.

Dehydrogenation performance of the Pt–Cu catalysts and the kinetic study

As shown in Fig. 4a–c, when the Pt loading was below 2.5%, the addition of Cu had the reverse effect. When the loading was greater than 2.5% and Pt : Cu = 10, a synergistic effect was observed. Also, the catalytic activity of Pt–Cu catalysts with higher loading was significantly higher than that of catalysts with lower loading, requiring less reaction time. This was

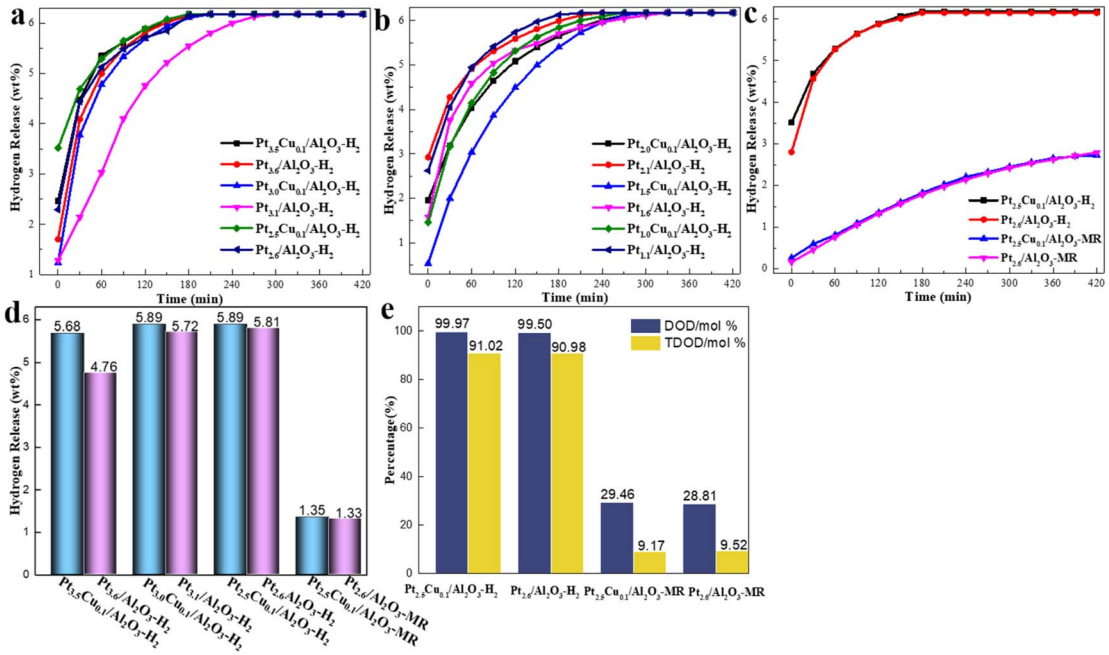

Fig. 4 Hydrogen release profiles of the dehydrogenation of 12H-MBT with (a–c) the prepared Pt–Cu/Al_2O_3 and Pt/Al_2O_3 catalysts from two preparation methods and different loading amounts of Pt with a reaction time of 6.5 h. (d) Comparison of the hydrogen release amount and (e) degree of dehydrogenation and total degree of dehydrogenation between the prepared Pt–Cu catalysts with a synergistic effect and Pt catalysts among the $Pt_{2.5}Cu_{0.1}/Al_2O_3$-MR/H_2 and related pure Pt catalysts at a reaction time of 2 h. Refer the reaction conditions in Section 2.4.

related to the number of active components. In Fig. 4d, it is clearly seen that the appropriate addition of Cu in a short period of time significantly improved the catalytic dehydrogenation performance of Pt. It further illustrated the synergistic catalytic effect between Pt (Pt $\geq$ 2.5wt%) and Cu. The best catalytic activity of catalyst A was selected for reactant analysis, as shown in Fig. 4e, and the effect of the reduction method on the dehydrogenation performance was compared. Finally, it was confirmed that the $Pt_{2.5}Cu_{0.1}/Al_2O_3$-H_2 catalyst could achieve 100% dehydrogenation (6.17 wt% hydrogen storage capacity), and the degree of complete dehydrogenation was closely related to the cracking of reactants. The above catalyst exhibited outstanding catalytic activity for 3 hours under the above reaction conditions, which can be explained as follows. On the one hand, the addition of Cu could have a "group effect" similar to that of additives (Re or Sn) in Pt reforming catalysts[39,40] for a lower Pt loading. It would actually have a greater impact on the catalytic performance of Pt components. The electronic and geometric effects of Cu are significant, which would actually weaken the catalytic dehydrogenation activity of Pt. On the other hand, Cu doping to form alloys and other surface dilution methods could disrupt the "cluster effect" for higher loading of Pt, especially for the $Pt_{2.5}Cu_{0.1}/Al_2O_3$ catalyst, which corresponded to the XRD and BET results (see Fig. S1 in the ESI).†

Competitive hydrogen spillover at Pt–Cu interfaces weakened 12H-MBT adsorption, promoting dehydrogenation product desorption through Pt site-interfacial synergy. Therefore, this could improve the dehydrogenation activity. Especially for the H_2-TPD, TEM, XRD, and *in situ* infrared spectra of the adsorption reaction of 12H-MBT on the $Pt_{2.5}Cu_{0.1}/Al_2O_3$ catalyst, this could also be demonstrated. Keane *et al.* also suggested that overflow hydrogen had an important promoting effect on the catalytic performance of Pt-like materials.[41] Fig. 4d further indicates that the 12H-MBT dehydrogenation activity was the highest on the $Pt_{2.5}Cu_{0.1}/Al_2O_3$-H_2 catalyst. At a reaction time of 3 hours, the dehydrogenation rate was close to 100% and the complete dehydrogenation rate was also relatively high. This was higher than that of $Pt_{2.6}/Al_2O_3$-H_2 and much higher than that of the $Pt_{2.5}Cu_{0.1}/Al_2O_3$-MR catalyst. Moreover, compared with the reported literature, the reaction time was significantly shortened.[15] In addition, the dehydrogenation rate of the $Pt_{2.5}Cu_{0.1}/Al_2O_3$-MR catalyst was higher than that of the $Pt_{2.6}/Al_2O_3$-MR catalyst within 3 hours on account of the fact that large metal particles are more conducive for substrate reaction in catalyzing the 12H-MBT dehydrogenation reaction. It was remarkable that the metal particle size of the $Pt_{2.5}Cu_{0.1}/Al_2O_3$-H_2 catalyst was larger than that of $Pt_{2.6}/Al_2O_3$ and $Pt_{2.6}/Al_2O_3$-MR, and the Pt grains doped with Cu were highly dispersed on the support. Meanwhile, Pt coexists with Cu and forms alloy interactions, while the $PtCu_x$ alloy further synergistically catalyzes the dehydrogenation reaction by coordinating with the negative C ions. Besides, the unique electronic structure of the Pt–Cu alloy facilitated the transfer of electrons from Pt to Cu and reduced the electron density of Pt. Thus, it suppressed excessive dehydrogenation and hydrogenation in the 12H-MBT cycle.

Fig. 5 shows the 12H-MBT's dehydrogenation activity data of Pt–Cu/Al_2O_3 and Pt/Al_2O_3 catalysts with various preparation methods and loading amounts at different temperatures. Compared with Pt/Al_2O_3-H_2 catalysts with the same total

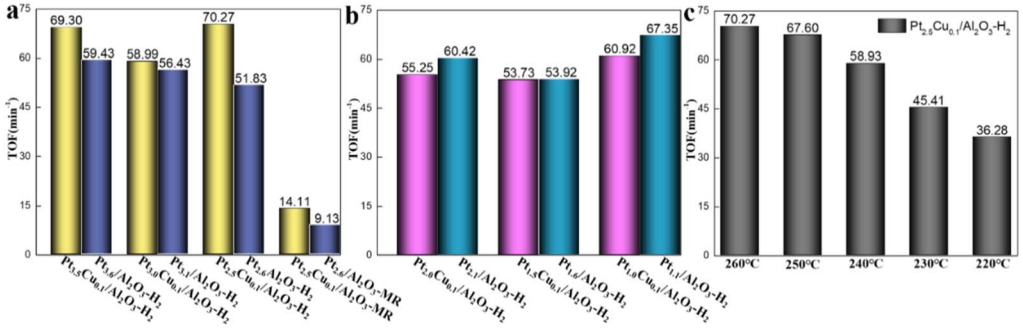

Fig. 5 Turnover frequency Part labels (TOF) of intermediates for the prepared Pt–Cu/Al_2O_3 catalyst with synergistic effect and Pt/Al_2O_3 catalysts from two preparation methods and different loading amounts of Pt at different temperatures in the early stage of the reaction.

loading, Pt–Cu/Al_2O_3 catalysts with high Pt loading (≥2.5 wt%) exhibited a higher 12H-MBT conversion rate, 0H-MBT yield, and TOF value. The $Pt_{2.5}Cu_{0.1}/Al_2O_3$-H_2 catalyst had a higher CO adsorption capacity than the $Pt_{2.6}/Al_2O_3$-H_2 catalyst. This indicated that the higher number of surface hydrogen adsorption active sites was responsible for its high intrinsic activity (TOF value). In addition, the intrinsic activity of the $Pt_{2.5}Cu_{0.1}/Al_2O_3$-H_2 catalyst (70.27 min^{-1}) was higher than that of other catalysts. This was due to the high dispersion on the metal surface and the increase in the number of active sites caused by the presence of Pt–Cu alloys. In addition, the reaction temperature also had significant influence on the activity. The results showed that the higher the temperature, the higher the intrinsic activity due to the presence of *in situ* hydrogen. The intrinsic activity of this catalyst was not significantly different at 250 °C and 260 °C. It indicated a further room for improvement in the subsequent dehydrogenation temperature reduction for the 12H-MBT system. Surprisingly, pure Pt catalysts also exhibited excellent intrinsic activity at low loading levels, providing another approach for subsequent research.

The corresponding kinetic analysis was conducted for unveiling the mechanism of the excellent catalytic dehydrogenation performance of the $Pt_{2.5}Cu_{0.1}/Al_2O_3$-H_2 catalyst on 12H-MBT. As shown in Fig. 6a, the dehydrogenation reaction rate of 12H-MBT increased with the increase in temperature. The substrate dehydrogenation rate was the fastest and the reaction degree was the most complete at 260 °C. When the temperature dropped to 220 °C, the final dehydrogenation amount at 390 minutes was about one-third of the final dehydrogenation amount at 260 °C. This indicated that the reaction was endothermic, and the increase in temperature was more conducive to the substrate reaction. Furthermore, the viscosity of the reaction substrate decreased with the increase in temperature. This was beneficial for better dispersion of the catalyst in the reaction system and sufficient contact with the 12H-MBT reaction substrate. It facilitated the mass transfer of hydrogen gas in the reaction phase as well, making it easier for hydrogen gas to overflow from the reaction system. Thus, this facilitated and accelerated the dehydrogenation reaction. Moreover, it could be observed from the graph that the dehydrogenation amount at 250 °C after 210 minutes of the reaction was roughly the same as that at 260 °C.

Thus, the $Pt_{2.5}Cu_{0.1}/Al_2O_3$-H_2 catalyst can effectively reduce the dehydrogenation temperature of the 12H-MBT system, implying that the catalyst could effectively reduce the reaction energy barrier. Meanwhile, in the initial stage of the dehydrogenation reaction, it conformed to the apparent first-order reaction where the reaction rate was proportional to the first power of the reactant concentration. The five straight lines could be linearly fitted from the initial reaction data of the five curves in Fig. 6a. The slope of the straight line corresponded to the apparent reaction rate constant k of the substrate dehydrogenation reaction at different temperatures, as shown in the fitting results in Fig. 6b–f.

From the calculation based on the data in Fig. 7a, the apparent activation energy (E_a) of the dehydrogenation reaction of 12H-MBT is 108.6 kJ mol^{-1}, which is relatively small and indicated the easy occurrence of the reaction. This was in line with the fitting results of the previous reaction kinetics model as well. This E_a value also confirmed that the catalytic reaction rate was mainly controlled by the catalytic conversion step instead of the diffusion process. Fig. 7b–f shows the concentration curves of intermediates during the dehydrogenation process of 12H-MBT by the $Pt_{2.5}Cu_{0.1}/Al_2O_3$-H_2 catalyst at different temperatures. This further comprehended the possible dehydrogenation mechanism with excellent catalytic activity and product formation.10H-MBT, 6H-MBT, 4H-MBT, and 0H-MBT could be detected using gas chromatography and gas chromatography-mass spectrometry for the analyzed intermediates. It could be noted from the graph that the concentration of the substrate 12H-MBT in the reaction at 220 °C and 230 °C showed a stable decrease. However, the concentration of 12H-MBT at 240 °C, 250 °C, and 260 °C showed a cliff like decrease within 210 minutes.

The complete dehydrogenation product, 0H-MBT, was nearly unobservable at low temperatures of 220–230 °C. The 0H-MBT concentration increased with reaction time as the reaction temperature increased to 240 °C, and the concentration significantly increased with time at 260 °C. This illustrated that the conditions required for the generation of 12H-MBT were more stringent. Regarding the 10H-MBT intermediate, with the progress of the reaction time, the reaction basically generated subsequent products at different reaction temperatures. Only a small part could be detected in the prophase reaction,

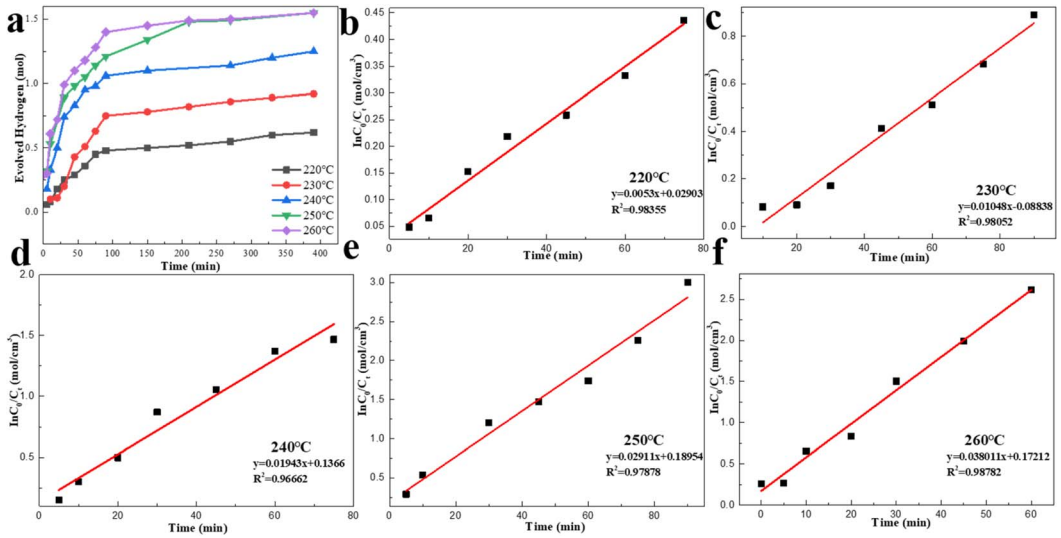

Fig. 6 Hydrogen release profiles (a) and linear fitting diagram of initial dehydrogenation reaction (b–f) of 12H-MBT at different temperatures over$Pt_{2.5}Cu_{0.1}/Al_2O_3$-H_2 catalyst.

indicating that the macroscopic first step of the dehydrogenation reaction was easy to occur. As for the 6H-MBT intermediate, its concentration showed the trend of first increasing and then decreasing with time at different temperature ranges. The reaction was completed at the lowest temperature of 220 °C and the highest temperature of 260 °C, indicating that its macroscopic second step dehydrogenation was also relatively simple. From the changes in the intermediate 4H-MBT, it is seen that the concentration slowly increased with time at 220 °C, and was basically undetectable at other temperatures. This indicated that it could not undergo dehydrogenation at low temperatures, combined with the concentration changes of 0H-MBT. With regard to other high temperatures, the final dehydrogenation product was not detected. These results collectively indicated that the last dehydrogenation step from 4H-MBT to 0H-MBT for this continuous dehydrogenation reaction had the most stringent reaction condition. The reaction was the slowest in the entire continuous dehydrogenation process as well, indicating that it was the rate determining step of the reaction.

Combined with the above experimental results, there was still a possibility for reduction for further exploration of the catalyst's effect on the dehydrogenation temperature of the system. The current detection methods could only detect intermediates in the dehydrogenation process of 12H-MBT, but

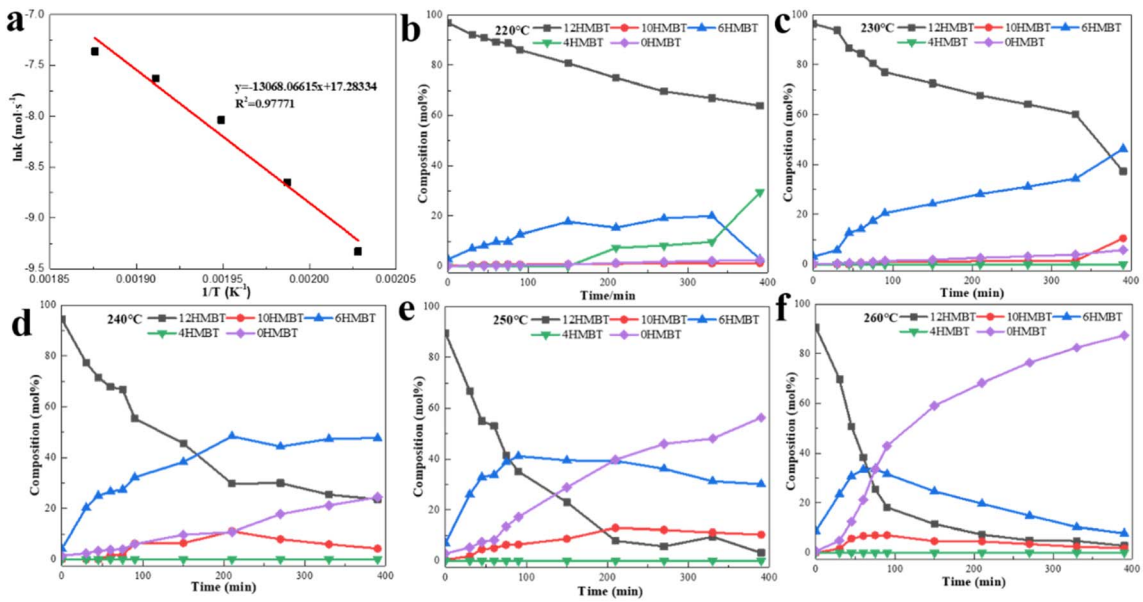

Fig. 7 (a) Relationship between ln k and $1/T$ in the initial stage of 12H-MBT dehydrogenation over the $Pt_{2.5}Cu_{0.1}/Al_2O_3$-H_2 catalyst. (b–f) Distribution of the dehydrogenation reaction product at different temperatures over the above catalyst.

their isomeric structures could not be detected. In summary, the dehydrogenation process of 12H-MBT under the action of the $Pt_{2.5}Cu_{0.1}/Al_2O_3$-H_2 catalyst is as follows: 12H-MBT → 10H-MBT → 6H-MBT → 4H-MBT → 0H-MBT. Theoretically, the dehydrogenation process mainly focused on one ring, and the starting position of dehydrogenation started from the most stable C^{3+}. Then, the position of the dehydrogenation double bond was located at the methylene group connected to the methyl group, and finally formed a large π bond. This process could be referred to other polycyclic aromatic hydrocarbon dehydrogenation processes.[42,43] In the complete dehydrogenation process of 12H-MBT, the reaction energy barrier was mainly concentrated in the R9-R12 step (counted by the number of H atoms removed). The following three most likely reaction paths are given and Path 1 had the lowest overall structural energy among them, and the rate-determining step was the release of the last two molecular H_2 for a 12H-MBT, *i.e.*, from 4H-MBT to 0H-MBT, as expressed by:

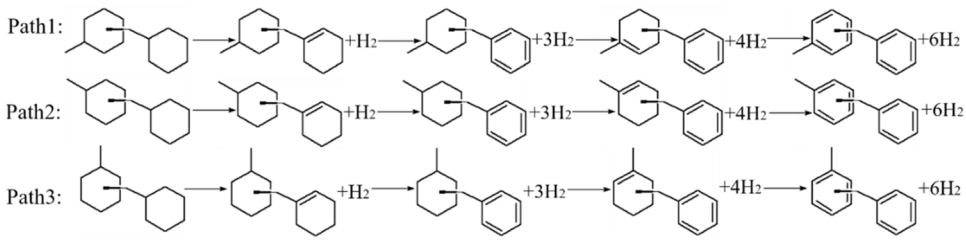

Mechanism of 12H-MBT dehydrogenation on $Pt_{2.5}Cu_{0.1}/Al_2O_3$-H_2 catalyst

DRIFT was adopted to study the surface adsorption and reaction process of the $Pt_{2.5}Cu_{0.1}/Al_2O_3$-H_2 catalyst using 12H-MBT as the probe in order to better understand the structure–activity relationship of this catalyst. The *in situ* infrared spectra of the reaction substrate molecules adsorbed on the $Pt_{2.5}Cu_{0.1}/Al_2O_3$-H_2 catalyst at different temperatures were compared. Also, the changes in the adsorption active species of 12H-MBT during dehydrogenation could determine the reaction mechanism on the $Pt_{2.5}Cu_{0.1}/Al_2O_3$-H_2 catalyst. In Fig. 8, the characteristic peaks of the adsorbed species are highlighted by subtracting the background from the *in situ* adsorption at room temperature on the $Pt_{2.5}Cu_{0.1}/Al_2O_3$-H_2 catalyst in N_2 gas. A certain change in the infrared spectrum was observed when the carrier gas switched from N_2 to the 12H-MBT mixture and adsorption was saturated at 25 °C. After further heating, the weak characteristic peaks at 2853 cm^{-1}, 2928 cm^{-1}, and 2974 cm^{-1} appeared (Fig. 6a), which corresponded to the C–H_2 symmetric stretching mode, C–H_2 asymmetric stretching mode, and C–H_3 asymmetric stretching mode, respectively. With the increase in temperature, the C–H_2 asymmetric stretching mode disappeared, and the intensity of other characteristic vibration mode peaks decreased. This explained that increasing temperature enabled the desorption or conversion of the 12H-MBT adsorbed species. It further confirmed that the catalyst was equipped with preeminent catalytic dehydrogenation activity for this reaction and the desorption energy was not too high at this time.

As the reaction temperature increased, the peak at 2140 cm^{-1} was attributed to the combined frequency peak of the C–H bending vibration and C=C symmetric stretching vibration in the low frequency range. A significant blue shift occurred, indicating that the coordination adsorption and activation of 12H-MBT on Pt and $PtCu_x$ active sites were the initial steps of the 12H-MBT dehydrogenation. The charge transfer and activation of H–H bonds might also have an impact on the subsequent reaction process, accompanied by further dehydrogenation.[44,45] In the low frequency range, the characteristic negative stretching vibration peak attributed to C=C

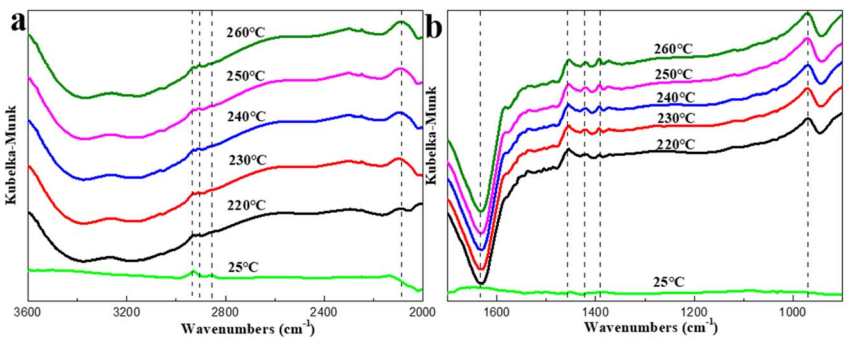

Fig. 8 12H-MBT-DRIFT spectra of the $Pt_{2.5}Cu_{0.1}/Al_2O_3$-H_2 catalyst ((a) 3600–2000 cm^{-1}, (b) 1700–900 cm^{-1}).

appeared around 1620 cm^{-1} in the spectrum from 220 °C to 260 °C and the intensity did not decrease significantly. This proved that the substrate underwent the dehydrogenation reaction at this site and the dehydrogenation process was relatively complex. It was found for the sample that at 1453 cm^{-1}, 1421 cm^{-1}, 1385 cm^{-1}, and 973 cm^{-1} (Fig. 6b), the former frequency corresponded to the C=C symmetric stretching vibration on the hexagonal ring. However, the latter three frequencies corresponded to the C–H bending vibration on the hexagonal ring. These characteristic peaks attested that the adsorption mode of 12H-MBT on the prepared samples was consistent with the previously reported Pt adsorption mode, both lying flat at the sample interface.[46,47]

All of the above suggested that the adsorption capacity of 12H-MBT on $Pt_{2.5}Cu_{0.1}/Al_2O_3$-H_2 was relatively strong, which did not significantly inhibit the dehydrogenation reaction of 12H-MBT. Moreover, the initial step of the 12H-MBT dehydrogenation was not the rate-determining step. The subsequent consecutive elementary reactions accompanied by the continuous dehydrogenation of the hexagonal ring to form the benzene ring derivatives were the real reaction energy barriers to be overcome. This was consistent with the experimental results.

Conclusion

In this study, the $Pt_{2.5}Cu_{0.1}/Al_2O_3$-H_2 catalyst with an alloy anchored by calcination exhibited excellent bimetallic synergistic catalytic activity for the 12H-MBT dehydrogenation. It was accompanied by the first complete reaction mechanism proposed to break the negative correlation between catalytic activity and selectivity. The comprehensive analyses, including XPS and HRTEM, indicated that the unique electron transfer alloy structure of Pt–Cu facilitated the transfer of electrons from Pt to Cu. It resulted in the electron migration between the metal and the support to significantly weaken SMSI, reducing the adsorption of aromatic products, and inducing appropriate H_2 adsorption. Highly dispersed Pt components in nanoparticles were related to the addition of Cu and the anchoring of metal components through calcination. This reduced the aggregation of Pt components, which facilitated the synergistic catalysis of bimetallic components. The unique electronic structure and spatial configuration of the synergistic catalytic mechanism between Pt and Cu lead to a dehydrogenation process, where the rate-determining step was the conversion from 4H-MBT to 0H-MBT.

Data availability

The data supporting this article have been included as part of the ESI.†

Author contributions

Qiuyue Ding: investigation, data collection, reaction test, writing – original draft preparation, Yixuan Zhang: catalytic test, reaction setup construction, discussion. Huijie Wei: reaction setup construction. Qing Li: catalyst preparation, characterization, paper revision. Yanyan Xi: catalyst characterization, discussion. Songqing Hu: research funding provision, writing and organization. Xufeng Lin: idea development, research funding provision, writing and organization.

Conflicts of interest

The authors declare no competing financial interest.

Acknowledgements

Supports from the National Natural Science Foundation of China (21576291) and from the Fundamental Research Funds for the Central Universities (23CX03007A) are gratefully acknowledged.

References

1 S. Ehteshami and S. H. Chan, *Energy Policy*, 2014, **73**, 103–109.
2 S. Niaz, T. Manzoor and A. H. Pandith, *Renewable Sustainable Energy Rev.*, 2014, **50**, 457–469.
3 N. Tsogt, D. Q. Gbadago and S. Hwang, *Energy Convers. Manage.*, 2024, **299**, 117856.
4 Z. Jiang, Q. Pan, J. Xu and T. Fang, *Int. J. Hydrogen Energy*, 2014, **3**(9), 17442–17451.
5 M. R. Usman, *Renewable Sustainable Energy Rev.*, 2022, **167**, 112743.
6 C. Sambo, A. Dudun, S. A. Samuel, P. Esenenjor and N. Muhammed, S and Haq B, *Int. J. Hydrogen Energy*, 2022, **47**(54), 22840–22880.
7 T. Y. Wei, K. L. Lim, Y. S. Tseng and S. L. I. Chan, *Renewable Sustainable Energy Rev.*, 2017, **79**, 1122–1133.
8 L. Lin, W. Zhou, R. Gao, S. Yao, X. Zhang, W. Xu and D. Ma, *Nature*, 2017, **544**, 80–83.
9 P. Modisha and D. Bessarabov, *Curr. Opin. Green Sustainable Chem.*, 2023, 100820.
10 J. H. Sinfelt, *J. Mol. Catal. A:Chem.*, 2000, **163**(1–2), 123–128.
11 J. Oh, T. W. Kim, K. Jeong, J. H. Park and Y. W. Suh, *ChemCatChem*, 2018, **10**(17), 3892–3900.
12 R. Lingayya, M. Vellakkaran, K. Nagaiah, J. B. Nanubolu and J. Asian, *Org. Chem.*, 2015, **4**(5), 462–469.
13 Y. Kwak, J. Kirk, S. Moon, T. Ohm, Y. J. Lee, M. Jang and Y. Kim, *Energy Convers. Manage.*, 2021, **239**, 114124.
14 N. Brückner, K. Obesser, A. Bösmann, D. Teichmann, W. Arlt, J. Dungs and P. Wasserscheid, *ChemSusChem*, 2014, **7**(1), 229–235.
15 X. Zhang, N. He, L. Lin, Q. Zhu, G. Wang and H. Guo, *Catal. Sci. Technol.*, 2020, **10**(4), 1171–1181.
16 B. Wang, Y. T. Chen, T. Y. Chang, Z. Jiang, Z. Q. Huang, S. Y. Wang and T. Fang, *Appl. Catal., B*, 2020, **266**, 118658.
17 S. Libin, Z. Yiming, Q. Suitao, S. Kevin J., T. Xiao, Y. Jiawei and Y. Chunhai, *ACS Catal.*, 2020, **10**(18), 10661–10671.
18 A. Corma, P. Reyes and J. A. Pajares, *React. Kinet. Catal. Lett.*, 1982, **18**(1–2), 79–84.

19 R. D. Hawthorn, G. H. Ackerman and A. C. Nixon, *AIChE J.*, 2010, **14**(1), 69–76.
20 L. Shi, S. Qi, J. Qu, T. Che, C. Yi and B. Yang, *Pergamon*, 2019, (11), 5345–5354.
21 F. Sotoodeh and K. J. Smith, *Ind. Eng. Chem. Res.*, 2010, **49**(3), 1018–1026.
22 A. Leinweber and K. Müller, *Energy Technol.*, 2018, **6**(3), 513–520.
23 Q. N. Dao, E. On, S. Ramadhani, K. Lee, H. Sohn, S. H. Choi and Y. Kim, *Int. J. Hydrogen Energy*, 2024, **56**, 1284–1293.
24 T. Pu, W. Zhang and M. Zhu, *Angew. Chem., Int. Ed.*, 2023, **62**(4), e202212278.
25 S. Park, M. M. Abdullah, K. Seong and S. Lee, *Chem. Eng. J.*, 2023, **474**, 145743.
26 S. Park, M. Naseem and S. Lee, *Materials*, 2021, **14**(24), 7613.
27 W. Lian, J. Wang, G. Wang, D. Gao, X. Li, Z. Zhang and B. Hou, *Fuel*, 2020, **268**, 117364.
28 J. Kibsgaard and T. F. Jaramillo, *Angew. Chem., Int. Ed.*, 2014, **53**(52), 14433–14437.
29 T. Takeguchi, W. Ueda, S. Manabe, R. Kikuchi, K. Eguchi, T. Kanazawa and S. Matsumoto, *Appl. Catal., A*, 2005, **293**, 91–96.
30 C. Dablemont, P. Lang, C. Mangeney, J. Y. Piquemal, V. Petkov, F. Herbst and G. Viau, *Langmuir*, 2008, **24**(11), 5832–5841.
31 P. Insorn and B. Kitiyanan, *Catal*, 2016, **6**(12), 199.
32 I. Tankov, W. H. Cassinelli, J. M. C. Bueno, K. Arishtirova and S. Damyanova, *Appl. Surf. Sci.*, 2012, **259**, 831–839.
33 H. Gao, W. Xu, H. He, X. Shi, X. Zhang and K. I. Tanaka, *Spectrochim. Acta, Part A*, 2008, **71**(4), 1193–1198.
34 Y. Ma, G. Xu, H. Wang, Y. Wang, Y. Zhang and Y. Fu, *ACS Catal.*, 2018, **8**(2), 1268–1277.
35 Z. Hooshmand, D. Le and T. S. Rahman, *Surf. Sci.*, 2017, **655**, 7–11.
36 O. Kortlüke and W. von Niessen, *Chem. Phys.*, 1999, **247**(2), 299–305.
37 A. L. Clauser, R. Giulian, Z. D. McClure, K. O. Sarfo, C. Ophus, J. Ciston and M. K. Santala, *Scr. Mater.*, 2020, **188**, 44–49.
38 X. H. Zhang, X. X. Li, H. Chen, T. B. Li, W. Su and S. D. Guo, *Mater. Des.*, 2016, **92**, 58–63.
39 C. Kim and G. A. Somorjai, *J. Catal.*, 1992, **134**(1), 179–185.
40 M. Ohta, Y. Ikeda and A. Igarashi, *Appl. Catal., A*, 2004, **266**(2), 229–233.
41 M. Keane and G. Tavoularis, *React. Kinet. Catal. Lett.*, 2003, **78**(1), 11–18.
42 Y. Dong, M. Yang, T. Zhu, X. Chen, G. Cheng, H. Ke and H. Cheng, *ACS Appl. Energy Mater.*, 2018, **1**(8), 4285–4292.
43 N. D. Huynh, S. H. Hur and S. G. Kang, *Int. J. Hydrogen Energy*, 2021, **46**(70), 34788–34796.
44 Y. Liu, A. Zhang, L. Xue, H. Zhang, Y. Hao, Y. Wang and S. Zeng, *ACS Appl. Energy Mater.*, 2021, **5**(1), 604–614.
45 Y. Liu, G. Wang and Y. Zhao, *Spectrochim. Acta, Part A*, 2023, **294**, 122482.
46 M. Amende, C. Gleichweit, K. Werner, S. Schernich, W. Zhao, M. P. Lorenz and J. Libuda, *ACS Catal.*, 2014, **4**(2), 657–665.
47 D. Arribas, V. Villalobos-Vilda, E. Tosi, P. Lacovig, A. Baraldi, L. Bignardi and P. Merino, *Nanoscale*, 2023, **15**(35), 14458–14467.